Energy & Environmental Science

RSC Publishing

PAPER

View Article Online
View Journal | View Issue

Organic solar cells featuring nanobowl structures

Cite this: *Energy Environ. Sci.*, 2013, **6**, 1192

Hung-Yu Wei,[a] Jen-Hsien Huang,[b] Chih-Yu Hsu,[c] Feng-Chih Chang,[d] Kuo-Chuan Ho*[ac] and Chih-Wei Chu*[be]

Received 19th November 2012
Accepted 30th January 2013

DOI: 10.1039/c3ee24128a

www.rsc.org/ees

Although organic solar cells having a bilayer configuration provide continuous conducting pathways for carrier transport to the requisite electrodes, their efficiencies have remained low because of the short exciton diffusion lengths of organic semiconductors. In this paper, we describe unique spatial organic solar cells featuring nanobowl array structures that capture more light and generate more power than planar organic solar cells. To construct bilayer solar cells, we used electrochemical deposition (with polystyrene beads as the template) to fabricate poly(3,4-ethylenedioxythiophene) nanobowl arrays, functioning as the hole extraction layer, on indium tin oxide substrates and then deposited copper phthalocyanine and a fullerene (C_{60} or C_{70}) to function as the active layer, onto the nanobowl arrays. By implementing this spatial structure, we could control the active layer's thickness, such that it would be suitable for exciton dissociation, while maintaining a high absorption of incident light (by increasing the absorber volume without decreasing the area of the donor–acceptor interface, such that the light path in the active layer was increased) and ensuring high exciton dissociation efficiency (by enlarging the donor–acceptor interface). Relative to an equally thick planar control active layer the photocurrent generated by such bilayer solar cells increased by approximately 90%.

1 Introduction

Organic solar cells (OSCs) are attracting attention for their potential applications in renewable energy because of their extraordinary low cost, light weight, and mechanical flexibility. In 1986, Tang[1] first developed small-molecule donor–acceptor (D–A) heterojunctions to dissociate strongly bound photogenerated excitons; since then, the power conversion efficiencies (PCEs) of OSCs have increased dramatically. Further increases in efficiency have been achieved in many different aspects of OSCs, including materials synthesis,[2,3] process control[4] and device architecture.[5–7] Recently, the PCEs of small-molecule heterojunction solar cells (SMHSCs) have reached in excess of 5%.[8,9] Although small molecules have many advantages for use in OSCs, including well-defined molecular structures, simple purification, and better batch-to-batch reproducibility, SMHSCs have received less attention because their performance continues to lag behind that of their bulk heterojunction counterparts.[10–14]

The ideal active layer in a heterojunction OSC should feature a large D–A interface, thereby allowing dissociation of every exciton generated within the active layer. In addition, the donor and acceptor materials should both feature continuous pathways through which their carriers can be transported to their respective electrodes.[15–17] A final requirement for the active layer should be that it is sufficiently thick to absorb a significant fraction of the sunlight. For OSCs featuring a heterojunction between two layers of neat materials, the carriers can always travel along continuous pathways to their corresponding electrodes, with the depositing sequence ensuring that each material is in contact with its correct electrode to minimize the carrier transport time and the probability of back electron transfer; nevertheless, the necessary compromise between photon absorption and carrier generation, due to the short exciton diffusion lengths (10–30 nm) and low carrier mobilities of organic semiconductors, will still limit the device performance.[18] Although thermal and solvent treatment can enlarge the D–A interface, resulting in increased power conversion efficiency (PCE),[19,20] such strategies are highly dependent on the nature of the materials—that is, not every material changes its morphology after solvent or thermal treatment. Intermixing layers can be introduced into OSCs to circumvent the trade-off between losses resulting from the limited absorption of thin layers and the recombination losses arising from thicker layers, leading to PCEs of greater than 6%.[2,3,21] Although the intermixing structure provides quite a large interface for exciton dissociation, the random distribution of donors and acceptors can result in inadequate percolation within

[a]*Institute of Polymer Science and Engineering, National Taiwan University, Taipei, 10617, Taiwan*

[b]*Research Center for Applied Sciences, Academia Sinica, Taipei, 11529, Taiwan. E-mail: gchu@gate.sinica.edu.tw*

[c]*Department of Chemical Engineering, National Taiwan University, Taipei, 10617, Taiwan. E-mail: kcho@ntu.edu.tw*

[d]*Department of Applied Chemistry, National Chao Tung University, Hsinchu, 30010, Taiwan*

[e]*Department of Photonics, National Chiao Tung University, Hsinchu, 300, Taiwan. E-mail: gchu@gate.sinica.edu.tw*

the bulk blend for carrier transport, potentially increasing the probability of carrier recombination and decreasing carrier mobilities. To solve those problems, many groups have investigated ordered bulk heterojunction (OBHJ) structures prepared by filling metal oxide nanostructures (*e.g.*, TiO_2, ZnO) with polymers.[22–30] OBHJ structures have distinct advantages over their disordered counterparts in that their morphologies can be controlled precisely and the organic semiconductors can retain their intrinsic transport properties. The efficiency of such systems is, however, moderate because of incompatibilities arising from the nanostructure dimensions of the metal oxide. Moreover, because the absorption of metal oxides in the visible region is minimal, it does not contribute much to the photocurrent.

An alternative, highly promising strategy toward increasing optical absorption is to employ periodic nanostructured electrodes or buffer layers. Many techniques can be used to form nanostructures on the hole transfer layer [poly(3,4-ethylenedioxythiophene):polystyrenesulfonate (PEDOT:PSS)], including nanoimprinting,[31] lithography,[32] direct laser interference patterning,[33] templating with patterning,[34,35] and the use of electrochemical polymerized nanostructure;[36] as a result, the active layer will adopt the shape of the nanostructured electrodes or buffer layers. Resulting improvements in PCE can be attributed to improvements in both optical and electrical properties. As light passes through the structure, its scattering increases the effective path in the active layer, thereby increasing the absorption relative to that for an active layer of the same thickness but lacking the nanostructural features. In addition, the structure possesses a graded refractive index, which effectively suppresses reflection, and a structure pitch that can be designed to match the carrier diffusion length and minimize charge loss through recombination. In this paper, we demonstrate a spatial OSC constructed on a periodic PEDOT nanobowl array. We fabricated periodic arrays of nanostructures by using electrochemical deposition to fill the interstitial sites of templating polystyrene (PS) beads with PEDOT, obtaining active layers with precisely defined shapes. Because the exciton diffusion length is limited at 10–30 nm,[37–42] the thickness of the active layer was restricted. An active layer having a nanobowl structure provides a longer light path and a larger D–A interface, and a greater absorber volume in the same projection area, leading to higher absorption and greater exciton dissociation than those obtained by a planar active layer at the same thickness.

2 Experimental

2.1 Fabrication of structured PEDOT film and structured active layer

The PS solution was prepared by adding colloidal particles (diameter: 400 nm; density: 1.05 g cm^{-3}; 9.7% solid; Bangs Laboratories Fishers, IN, USA; 1.35 mL) into a dispersion solution (Triton X-100–MeOH, 1 : 100; 1.00 mL). The PS solution was spin-coated onto the ITO substrate using a two-step procedure (10 rpm for 20 s, then 1500 rpm for 40 s) to form an ordered template. The ITO substrate presenting well-ordered PS beads was stored overnight so that the PS beads could form a more-organized, fixed template.[43,44]

The PEDOT layer was electrodeposited onto the ITO substrate presenting the ordered PS beads by applying a potential of 1.0 V (*vs.* Ag/AgCl), using a Pt counter electrode, until a charge density of 2 mC cm^{-2} was reached. The bath solution was deionized water containing 0.1 M $LiClO_4$ (Aldrich, 95+%), 0.01 M 3,4-ethylenedioxythiophene (EDOT, Aldrich), and 1 wt% sodium dodecyl sulfate (SDS) as a surfactant. After the PEDOT film had been deposited, the substrate was immersed in pure toluene for 12 h to remove the PS beads. The remaining PEDOT film possessed a bowl-like structure.[45,46]

CuPc layers (as the p-type layer) having thicknesses ranging from 20 to 60 nm were deposited (thermal evaporation) along the structured PEDOT; 40 nm C_{60} (or C_{70}), as the n-type layer, was subsequently deposited. A 60 nm Al cathode was deposited on the fullerene layer. The whole device was then transferred to a hot plate and annealed at 150 °C for 20 min.

2.2 Morphology and material characterizations

Surface morphologies of the nanostructures were measured using a scanning electron microscope (FEI Nova 200) and an atomic force microscope (Veeco di Innova). Cyclic voltammetry was performed using a three-electrode cell with 0.5 M $LiClO_4$ in MeCN as the electrolyte; a fabricated PEDOT film as the working electrode; a Pt sheet as the counter electrode; and nonaqueous Ag/Ag^+ (containing 0.01 M $AgNO_3$ and 0.1 M $TBAClO_4$ in MeCN) as the reference electrode. Spectroelectrochemical data were recorded using a Shimadzu UV-1601PC spectrophotometer. Ultraviolet photoemission spectroscopy was performed using a PHI 5000 VersaProbe (ULVAC-PHI, Chigasaki, Japan). UV-Vis absorption spectra were recorded using a Jasco ISN-723 integrating sphere that analyzed reflected light. A plane surface with diffuse-reflection MgO coating was used to prevent the light passing through the sample. External quantum efficiencies (EQEs) were measured by comparing the photocurrent of a sample device and a standard Si device at different wavelengths of incident light.

3 Results and discussion

Fig. 1(a) illustrates the fabrication of the spatial active layer. In this approach, a planar D–A interface forms merely a circular plane, whereas the D–A interface along the bowl-like structure is a hemisphere in the same projected area normal to the device. Hence, the D–A interface for a planar active layer is πR^2, whereas it is $2\pi R^2$ for a spatial active layer. Because the optimized active layer thickness for a bilayer solar cell is usually close to 100 nm,[47,48] the nanobowl features would be fully covered by the subsequently deposited active layers if the diameter of each bowl were less than 200 nm. On the other hand, the height of the bowl-like structure is half the diameter of the beads. Considering the thickness of the active layer, larger PS beads would create nanobowls having sharp edges and a rough surface; such an active layer would not fully cover the surface of the structured PEDOT and would, thereby, lead to a short circuit; therefore in this study we employed 400 nm PS beads to maintain the nanobowl features and prevent short

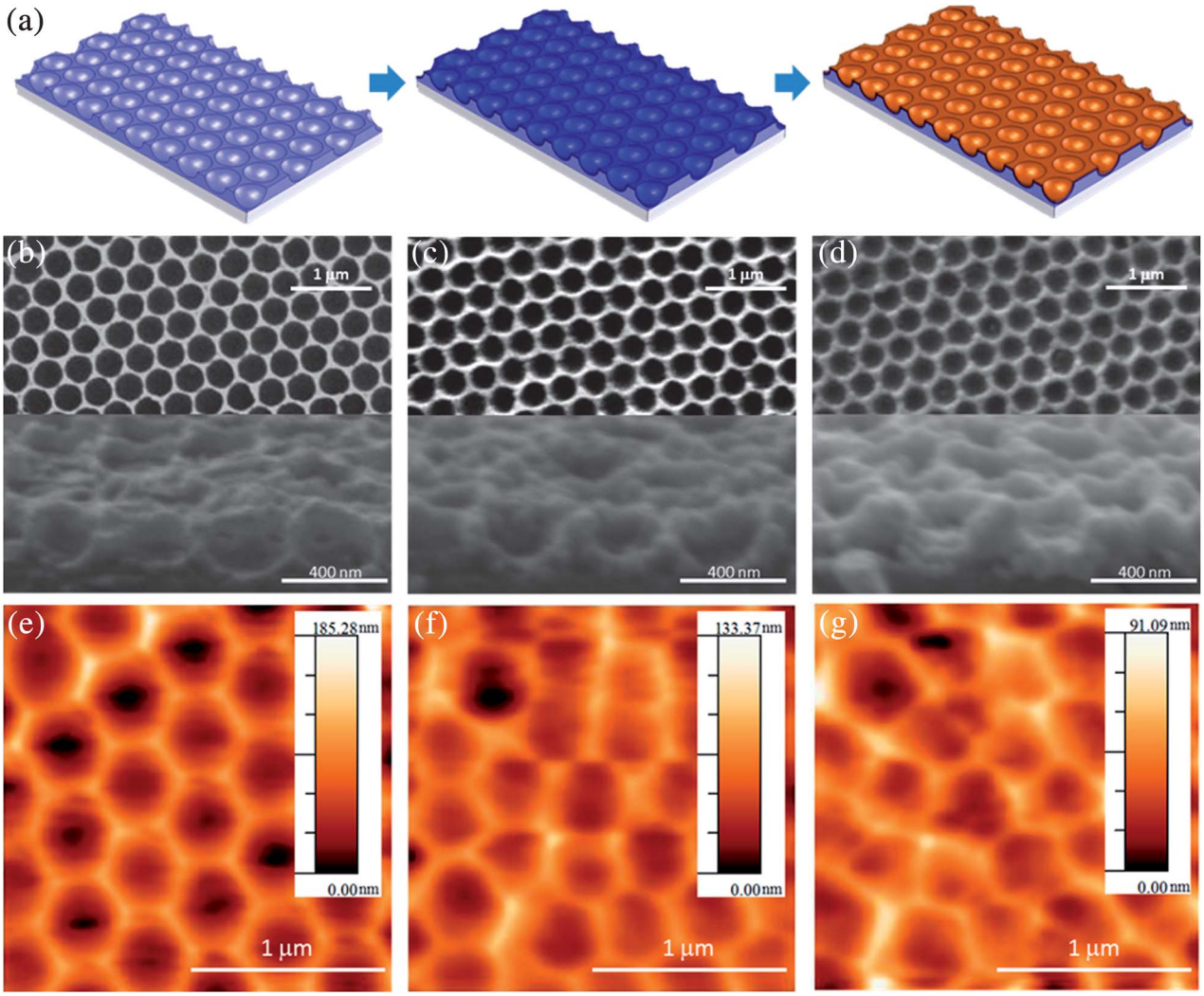

Fig. 1 (a) Schematic representation of the fabrication of a nanostructured active layer. (b–d) Top-view SEM images of (b) the as-prepared PEDOT structure and (c and d) the structures obtained after deposition of (c) 40 nm CuPc and (d) 40 nm CuPc (40 nm)/C_{60} (40 nm); insets: cross-sectional views. (e–g) Corresponding AFM images.

circuiting. After depositing a 40 nm film of CuPc and a 40 nm film of C_{60} (or C_{70}), we used scanning electron microscopy (SEM) to characterize the surface features [Fig. 1(b)–(d)]. Although the thermal deposition process allowed the active materials to cover the PEDOT surface, the features of the nanobowls remained; that is, they were not filled up by the coating of the active layer materials, as evidenced in Fig. 1(d). We recorded cross-sectional SEM images of the PEDOT nanobowl structures before and after depositing the active layer [insets of Fig. 1(b)–(d)], observing that the materials were deposited with precisely defined shapes; as the walls of the nanobowls became increasingly thicker, the active layer fully covered the nanobowl PEDOT surface, suggesting that short circuiting would be prevented. Fig. 1(e)–(g) display the morphologies of the nanobowl PEDOT, CuPc, and C_{60} layers, as analyzed using atomic force microscopy (AFM). The height of the features in the pristine nanobowl PEDOT layer was approximately 185 nm, close to half of the PS bead diameter. Although the features of the CuPc and C_{60} layers formed on the PEDOT gradually decreased in height, the bowl-like features remained evident, consistent with the cross-sectional SEM images.

Fig. 2 presents the current density (J)–voltage (V) characteristics of the four devices, CuPC/C_{60}/planar PEDOT, CuPC/C_{60}/structured PEDOT, CuPC/C_{70}/planar PEDOT, and CuPC/C_{70}/structured PEDOT, measured under 100 mW cm^{-2} air mass (AM) 1.5G solar simulated light. Table 1 summarizes the photovoltaic properties of these solar cells. As expected, the open circuit voltage (V_{OC}) remained constant for all devices. The short circuit current (J_{SC}) and fill factor (FF) of the solar cell featuring CuPc/C_{60} as the active layer both increased dramatically, from 4 to 7.37 mA cm^{-2} and from 45.2 to 55.9%, respectively, after introducing the structured PEDOT; accordingly, the PCE of this solar cell increased from 0.9 to 2.0%. In addition, the series resistances of the device decreased after employing the structured PEDOT. This behavior arose because the charge carriers will travel along the path providing the lowest resistance in PEDOT layer. Thus, in the case of planar PEDOT, the charge carriers passed through the

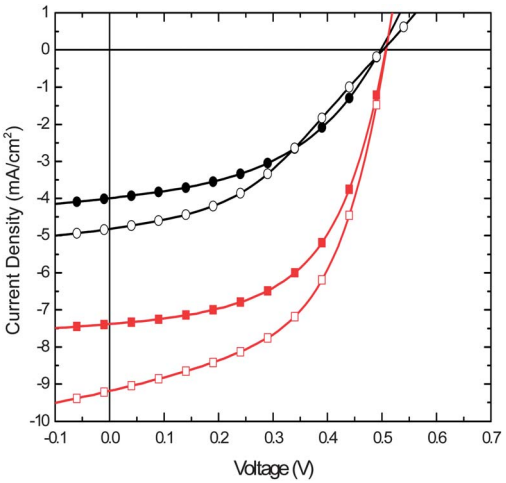

Fig. 2 Current density–voltage (*J–V*) characteristics of four devices: CuPc/C_{60} planar active layer (solid black), CuPc/C_{60} structured active layer (solid red), CuPc/C_{70} planar active layer (open black), and CuPc/C_{70} structured active layer (open red).

entire thickness of the PEDOT layer; for our bowl-like PEDOT, however, the distance between the CuPc/PEDOT interface and the PEDOT/ITO interface was not uniform. At regions of thin PEDOT, the charge carriers would pass directly through the PEDOT film to reach the ITO surface, but at regions of thick PEDOT the charge carriers might transfer along the PEDOT surface for a distance and then penetrate through a region of thin PEDOT to reach the ITO – if doing so is the path with the lowest resistance among all possible routes. Thus we get lower series resistances in device while incorporating structured PEDOT, resulting in improving the FF.

The low absorption of C_{60} results from its high degree of symmetry, which makes the lowest-energy transitions formally dipole forbidden. Therefore, when we replaced C_{60} with a less-symmetrical fullerene, C_{70}, these transitions became allowed and provided a dramatic increase in light absorption,[49] manifested by a further increase in PCE to 2.5%. To clarify the cause of the increase in J_{SC} after introducing the structured PEDOT, we recorded UV-Vis absorption spectra to determine the absorption capabilities of spatial and planar active layers of the same thickness. Fig. 3(a) reveals that although the characteristic peaks appeared at essentially the same wavelengths, the absorption of the active layer deposited on the structured PEDOT was much higher than that on the planar PEDOT. The higher absorption of the spatial devices relative to the planar devices is consistent with the large differences in their values of J_{SC}.

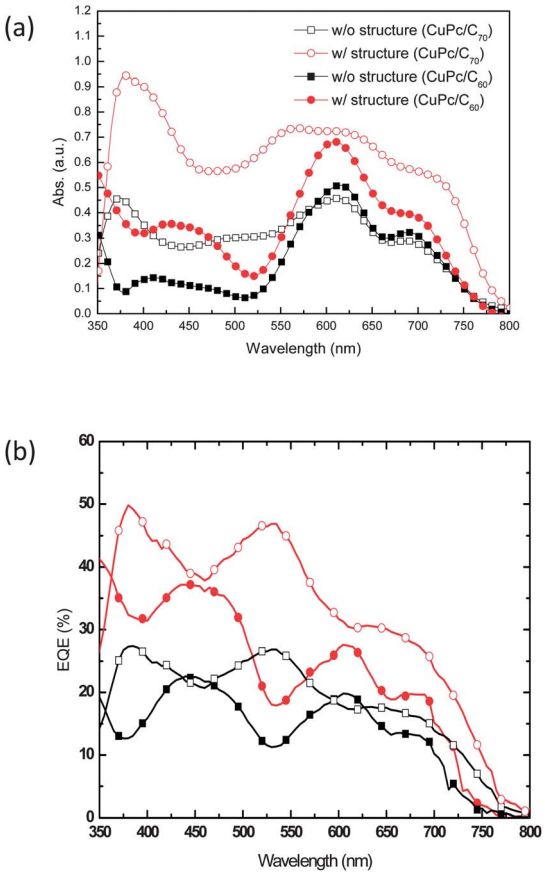

Fig. 3 (a) Absorption and (b) EQE spectra of active layers comprising CuPc/C_{60} (black) and CuPc/C_{70} (red) in the presence (open dots) and absence (solid dots) of the structure.

We suspected that the photocurrent might be enhanced not only from the increased light path but also other optical effects. To understand the influence of the structured PEDOT on the increased value of J_{SC}, we measured the external quantum efficiencies (EQEs) for the four devices [Fig. 3 (b)]. The EQE of the device featuring the nanostructures was almost twice that of the planar device over a wide range of wavelengths (350–800 nm), consistent with its improved value of J_{SC}. Because the EQE curves of the devices prepared with and without a structured active layer were sensitive to the wavelength of incoming light, trapping and reabsorption of reflected light were probably not the main factors influencing the values of J_{SC}.

Considering the anti-reflection effect of the nanostructure, we also investigated the cell performances in response to light at

Table 1 Photovoltaic properties of the four devices: CuPc/C_{60} planar active layer, CuPc/C_{60} structured active layer, CuPc/C_{70} planar active layer, and CuPc/C_{70} structured active layer

	V_{OC} (V)	J_{SC} (mA cm^{-2})	FF (%)	PCE (%)	R_s (Ω)	R_{sh} (kΩ)
Planar PEDOT/CuPc/C_{60}/Al	0.5	4.00	45.2	0.904	43.7	6.14
Planar PEDOT/CuPc/C_{70}/Al	0.5	4.82	40.1	0.966	37.0	4.55
Structured PEDOT/CuPc/C_{60}/Al	0.5	7.37	55.9	2.061	14.6	11.9
Structured PEDOT/CuPc/C_{70}/Al	0.5	9.18	53.8	2.469	9.35	3.22

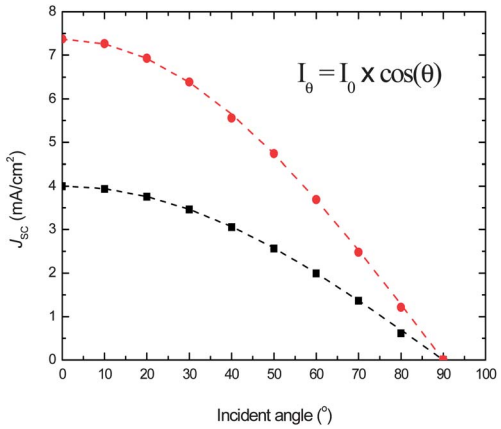

Fig. 4 Current density variations with respect to the incident angle of light. The devices incorporated CuPc/C_{60} (red dots: with structure; black dots: without structure; dashed lines: simulated value of current by cosine law at different angles).

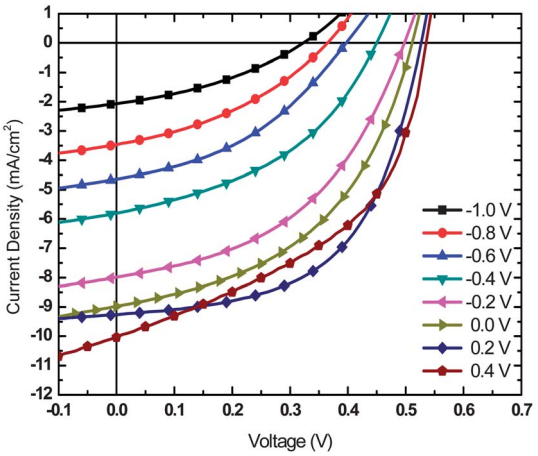

Fig. 5 Current density–voltage (*J–V*) characteristics of devices incorporating structured active layers deposited on PEDOT layers that had been subjected to various biases.

various incident angles (Fig. 4). The current densities of both devices, regardless of the presence or absence of the structured active layer, obeyed the cosine law ($I_\theta = I_0 \times \cos\theta$).[50] If the nanostructure exhibited any anti-reflection effects, we would expect the absorption spectra to feature fewer valleys at certain wavelengths.[51] Because the absorption spectra of the devices featuring the structured PEDOT had the same characterization peaks (and valleys) as those of the devices prepared without the structured PEDOT, and because the photocurrents at large angles were no greater than the theoretical values from the cosine law, we conclude that the structure did not exert a remarkable anti-reflection effect, possibly because the similar refractive indices of PEDOT (1.4–1.6) and CuPc (*ca.* 1.5)[52,53] led to almost no refractive index gradient in the region of the structured hole extraction layer and the active layer. Accordingly, we believe that the enhancement in current density resulted from the larger junction D–A interface and the elongated light path in the active layer. We suspect that if we were to employ a donor material having a refractive index much greater than 1.5, the light trapping would contribute to more efficient light absorption, resulting in further increase in cell efficiency. Deposition of a silver thin film along the nanostructure provides a plasmonic effect that can increase the absorption of the active layer in both organic and inorganic solar cell system.[54–56]

PEDOT is an electrochromic material that can be switched from its oxidized transparent light-blue state to its reduced dark-blue state; its optical and electrical properties can be tuned electrochemically upon applying different biases in lithium perchlorate electrolytes.[57,58] To further optimize the device performance, we tested the effect of the applied bias on the structured PEDOT layers prior to depositing the active layer. Fig. 5 displays the *J–V* characteristics of devices featuring a structured PEDOT under various treated biases.

The device performance changed significantly upon varying the treated bias; Table 2 summarizes the photovoltaic parameters. Tuning the treated bias from −1 to +0.4 V, we found that the values of J_{SC} and V_{OC} increased monotonously from 2.07 to 10.03 mA cm^{-2} and from 0.32 to 0.53 V, respectively. We limited the oxidation potential to +0.4 V (*vs.* Ag/Ag$^+$ in acetonitrile) because the overoxidation starting potential was approximately +0.5 V (*vs.* Ag/Ag$^+$ in MeCN). Electrochemical overoxidation is a rapid process that can permanently reduce the electronic conductivity of polythiophenes; indeed, we observed decreasing device performance prior to the physical properties of the PEDOT film becoming irreversible.[45] The transmittance spectra of the PEDOT film recorded at applied biases ranging from −1.0 to +0.4 V reveal [Fig. 6] that the PEDOT films behaved as semiconducting materials (having optical band gaps and lower transmission) when they were subjected to greater reduction (negative) biases and as conducting materials (higher transmission) when they were treated with greater oxidation (positive) biases. The increasing transmission upon increasing the applied oxidation bias is in good agreement with the monotonous increase in the value of J_{SC}.

The absolute values of the highest occupied molecular orbital (HOMO) energy level were determined by measuring the shift in the secondary electron cutoff from the ultraviolet photoemission spectra of the PEDOT films subjected to different biases. We observe a clear trend: the HOMO energy levels of the PEDOT films decreased from 5.20 eV when the applied bias was +0.4 to 4.16 eV when the applied bias was −1 V. Upon varying the applied biases from −1 to +0.2 V, the values of V_{OC} and FF of the corresponding devices increased from 0.32 V and 35.6% to 0.52 V and 56.5%, respectively, consistent with the shift in the HOMO energy level. Moreover, the higher HOMO energy level resulted in a decreased energy barrier for carrier collection and, therefore, increased values of J_{SC} and FF. Although the PEDOT film subjected to a bias of +0.4 V provided a higher HOMO energy level and greater transmission, leading to even higher values of V_{OC} and J_{SC}, respectively, the conductivity of the hole transport layer was too high, resulting in decreased shunt resistance and, therefore, a decreasing FF (Fig. 5 and Table 2). Combining the effects of the nanostructure and electrochemical treatment, the highest-performing device exhibited values of V_{OC}, J_{SC}, and FF of 0.52 V, 9.26 mA cm^{-2}, and 56.5%, resulting in a PCE of 2.72% under AM 1.5G illumination.

Table 2 Photovoltaic properties of the solar cell devices incorporating structured active layers deposited on PEDOT layers that had been subjected to various biases

Treated potential (*vs.* Ag/Ag^+)	V_{OC} (V)	HOMO (eV)	J_{SC} (mA cm^{-2})	FF (%)	PCE (%)	R_s (Ω)	R_{sh} (kΩ)
−1.0	0.32	−4.16	2.07	35.6	0.236	32.9	3.64
−0.8	0.36	−4.27	3.47	38.1	0.467	26.3	2.79
−0.6	0.39	−4.35	4.64	40.5	0.733	27.7	3.08
−0.4	0.44	−4.46	5.80	43.0	1.097	17.5	2.69
−0.2	0.49	−4.62	7.99	46.2	1.809	21.9	3.07
0.0	0.50	−4.83	8.98	48.1	2.158	17.7	3.68
0.2	0.52	−5.01	9.26	56.5	2.720	11.4	5.06
0.4	0.53	−5.20	10.03	46.6	2.487	2.25	1.78

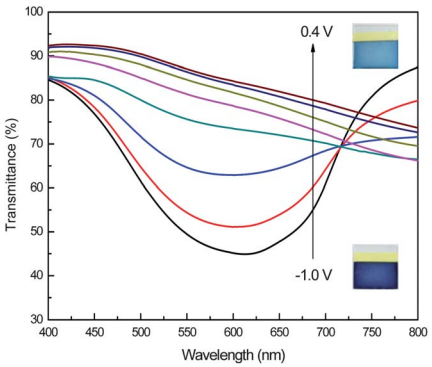

Fig. 6 Transmittance spectra of PEDOT under different applied potentials (*vs.* Ag/Ag^+ in 0.1 M $LiClO_4$).

4 Conclusions

Relative to planar bilayer OSCs, those possessing an active layer having a nanobowl structure can feature a significantly increased light path in the active layer, thereby enhancing the absorption of incident light, and a mathematical doubling of the D–A interface, thereby increasing the carrier collection efficiency, resulting in higher photocurrent generation. At the same thickness of the CuPc/C_{70} active layer, we obtained a PCE of 2.47% from an OSC device incorporating a nanobowl active layer, in contrast to a value of only 0.97% for the corresponding device possessing a planar active layer. To further optimize the device efficiency, the electrical and optical properties of the PEDOT film could be tuned by applying potentials prior to depositing the active layer. The highest performance appeared when we treated the PEDOT film under an applied bias of +0.2 V prior to depositing the active layer; the efficiency of these CuPc/C_{70}-based solar cells reached as high as 2.72%. By combining the benefits of high absorption and a large D–A interface, such nanobowl structures might open a new route toward next-generation, high-efficiency, low-cost organic photovoltaic systems.

Acknowledgements

We thank the National Science Council (NSC), Taiwan (NSC100-2221-E-001-009 and NSC100-2120-M-009-004), and the Academia Sinica research program on nanoscience and nanotechnology for financial support.

References

1 C. W. Tang, *Appl. Phys. Lett.*, 1986, **48**, 183.
2 Y. H. Chen, L. Y. Lin, C. W. Lu, F. Lin, Z. Y. Huang, H. W. Lin, P. H. Wang, Y. H. Liu, K. T. Wong, J. Wen, D. J. Miller and S. B. Darling, *J. Am. Chem. Soc.*, 2012, **134**, 13616–13623.
3 S.-W. Chiu, L.-Y. Lin, H.-W. Lin, Y.-H. Chen, Z.-Y. Huang, Y.-T. Lin, F. Lin, Y.-H. Liu and K.-T. Wong, *Chem. Commun.*, 2012, **48**, 1857–1859.
4 F. Yang, M. Shtein and S. R. Forrest, *Nat. Mater.*, 2005, **4**, 37–41.
5 K. Tvingstedt, V. Andersson, F. Zhang and O. Inganäs, *Appl. Phys. Lett.*, 2007, **91**, 123514.
6 Y. Zhou, F. Zhang, K. Tvingstedt, W. Tian and O. Inganäs, *Appl. Phys. Lett.*, 2008, **93**, 033302.
7 M. Bernardi, N. Ferralis, J. H. Wan, R. Villalon and J. C. Grossman, *Energy Environ. Sci.*, 2012, **5**, 6880–6884.
8 J. Xue, S. Uchida, B. P. Rand and S. R. Forrest, *Appl. Phys. Lett.*, 2004, **85**, 5757–5759.
9 J. Xue, B. P. Rand, S. Uchida and S. R. Forrest, *Adv. Mater.*, 2005, **17**, 66–71.
10 L. Dou, W.-H. Chang, J. Gao, C.-C. Chen, J. You and Y. Yang, *Adv. Mater.*, 2012, **25**, 825–831.
11 C.-H. Chung, T.-B. Song, B. Bob, R. Zhu, H.-S. Duan and Y. Yang, *Adv. Mater.*, 2012, **24**, 5499–5504.
12 Y. He, J. You, L. Dou, C.-C. Chen, E. Richard, K. C. Cha, Y. Wu, G. Li and Y. Yang, *Chem. Commun.*, 2012, **48**, 7616–7618.
13 L. Dou, J. Gao, E. Richard, J. You, C.-C. Chen, K. C. Cha, Y. He, G. Li and Y. Yang, *J. Am. Chem. Soc.*, 2012, **134**, 10071–10079.
14 Y. He, C. Chen, E. Richard, L. Dou, Y. Wu, G. Li and Y. Yang, *J. Mater. Chem.*, 2012, **22**, 13391–13394.
15 K. M. Coakley and M. D. McGehee, *Chem. Mater.*, 2004, **16**, 4533–4542.
16 P. K. Watkins, A. B. Walker and G. L. B. Verschoor, *Nano Lett.*, 2005, **5**, 1814–1818.
17 R. A. Marsh, C. Groves and N. C. Greenham, *J. Appl. Phys.*, 2007, **101**, 083509–083507.
18 P. Peumans, A. Yakimov and S. R. Forrest, *J. Appl. Phys.*, 2003, **93**, 3693.
19 G. Wei, X. Xiao, S. Wang, J. D. Zimmerman, K. Sun, V. V. Diev, M. E. Thompson and S. R. Forrest, *Nano Lett.*, 2011, **11**, 4261–4264.

20 D. Kekuda, J.-H. Huang, K.-C. Ho and C.-W. Chu, *J. Phys. Chem. C*, 2010, **114**, 2764–2768.
21 G. Chen, H. Sasabe, Z. Wang, X. F. Wang, Z. Hong, Y. Yang and J. Kido, *Adv. Mater.*, 2012, **24**, 2768–2773.
22 S. S. Williams, M. J. Hampton, V. Gowrishankar, I. K. Ding, J. L. Templeton, E. T. Samulski, J. M. DeSimone and M. D. McGehee, *Chem. Mater.*, 2008, **20**, 5229–5234.
23 Z. Fan, H. Razavi, J.-w. Do, A. Moriwaki, O. Ergen, Y.-L. Chueh, P. W. Leu, J. C. Ho, T. Takahashi, L. A. Reichertz, S. Neale, K. Yu, M. Wu, J. W. Ager and A. Javey, *Nat. Mater.*, 2009, **8**, 648–653.
24 M. Grätzel, *Curr. Opin. Colloid Interface Sci.*, 1999, **4**, 314–321.
25 D. C. Olson, J. Piris, R. T. Collins, S. E. Shaheen and D. S. Ginley, *Thin Solid Films*, 2006, **496**, 26–29.
26 L. E. Greene, M. Law, D. H. Tan, M. Montano, J. Goldberger, G. Somorjai and P. Yang, *Nano Lett.*, 2005, **5**, 1231–1236.
27 L. E. Greene, M. Law, B. D. Yuhas and P. Yang, *J. Phys. Chem. C*, 2007, **111**, 18451–18456.
28 J. Chen, C. Li, J. L. Song, X. W. Sun, W. Lei and W. Q. Deng, *Appl. Surf. Sci.*, 2009, **255**, 7508–7511.
29 K. Yu and J. Chen, *Nanoscale Res. Lett.*, 2009, **4**, 1–10.
30 Z. Fan, D. J. Ruebusch, A. A. Rathore, R. Kapadia, O. Ergen, P. W. Leu and A. Javey, *Nano Res.*, 2009, **2**, 829–843.
31 W.-Y. Chou, J. Chang, C.-T. Yen, F.-C. Tang, H.-L. Cheng, M.-H. Chang, S. Lien-Chung Hsu, J.-S. Chen and Y.-C. Lee, *Appl. Phys. Lett.*, 2011, **99**, 183108.
32 J. B. Emah, R. J. Curry and S. R. P. Silva, *Appl. Phys. Lett.*, 2008, **93**, 103301.
33 L. Müller-Meskamp, Y. H. Kim, T. Roch, S. Hofmann, R. Scholz, S. Eckardt, K. Leo and A. F. Lasagni, *Adv. Mater.*, 2012, **24**, 906–910.
34 S.-Y. Chen, Y.-T. Yen, Y.-Y. Chen, C.-S. Hsu, Y.-L. Chueh and L.-J. Chen, *RSC Adv.*, 2012, **2**, 1314–1317.
35 T. Darmanin, H. Bellanger, F. Guittard, P. Lisboa, M. Zurn, P. Colpo, D. Gilliland and F. Rossi, *RSC Adv.*, 2012, **2**, 1033–1039.
36 H. Yang, Q. Song, Z. Lu, C. Guo, C. Gong, W. Hu and C. M. Li, *Energy Environ. Sci.*, 2010, **3**, 1580–1586.
37 T. J. Savenije, J. M. Warman and A. Goossens, *Chem. Phys. Lett.*, 1998, **287**, 148–153.
38 H. Becker, S. E. Burns and R. H. Friend, *Phys. Rev. B: Condens. Matter Mater. Phys.*, 1997, **56**, 1893–1905.
39 T. J. Savenije, M. J. W. Vermeulen, M. P. de Haas and J. M. Warman, *Sol. Energy Mater. Sol. Cells*, 2000, **61**, 9–18.
40 J. E. Kroeze, T. J. Savenije, M. J. W. Vermeulen and J. M. Warman, *J. Phys. Chem. B*, 2003, **107**, 7696–7705.
41 W. Kylberg, P. Sonar, J. Heier, J.-N. Tisserant, C. Muller, F. Nuesch, Z.-K. Chen, A. Dodabalapur, S. Yoon and R. Hany, *Energy Environ. Sci.*, 2011, **4**, 3617–3624.
42 Z. Wang, D. Yokoyama, X.-F. Wang, Z. Hong, Y. Yang and J. Kido, *Energy Environ. Sci.*, 2013, **6**, 249–255.
43 C. W. Kuo, K. H. Wei, C. H. Lin, J. Y. Shiu and P. Chen, *Electrophoresis*, 2008, **29**, 2931–2938.
44 C. W. Kuo, J. Y. Shiu, F. C. Chien, S. M. Tsai, D. Y. Chueh and P. Chen, *Electrophoresis*, 2010, **31**, 3152–3158.
45 T.-H. Lin and K.-C. Ho, *Sol. Energy Mater. Sol. Cells*, 2006, **90**, 506–520.
46 H.-Y. Wei, Y.-S. Hsiao, J.-H. Huang, C.-Y. Hsu, F.-C. Chang, P. Chen, K.-C. Ho and C.-W. Chu, *RSC Adv.*, 2012, **2**, 4746–4753.
47 G. Yu, J. Gao, J. C. Hummelen, F. Wudl and A. J. Heeger, *Science*, 1995, **270**, 1789–1791.
48 H. Shen, P. Bienstman and B. Maes, *J. Appl. Phys.*, 2009, **106**, 073109–073105.
49 J. W. Arbogast and C. S. Foote, *J. Am. Chem. Soc.*, 1991, **113**, 8886–8889.
50 J. L. Balenzategui and F. Chenlo, *Sol. Energy Mater. Sol. Cells*, 2005, **86**, 53–83.
51 J. Zhu, Z. Yu, G. F. Burkhard, C.-M. Hsu, S. T. Connor, Y. Xu, Q. Wang, M. McGehee, S. Fan and Y. Cui, *Nano Lett.*, 2008, **9**, 279–282.
52 B. Ruhstaller, S. A. Carter, S. Barth, H. Riel, W. Riess and J. C. Scott, *J. Appl. Phys.*, 2001, **89**, 4575.
53 E. Tutiš, M. N. Bussac, B. Masenelli, M. Carrard and L. Zuppiroli, *J. Appl. Phys.*, 2001, **89**, 430.
54 V. E. Ferry, M. A. Verschuuren, H. B. T. Li, R. E. I. Schropp, H. A. Atwater and A. Polman, *Appl. Phys. Lett.*, 2009, **95**, 183503–183503.
55 N. N. Lal, B. F. Soares, J. K. Sinha, F. Huang, S. Mahajan, P. N. Bartlett, N. C. Greenham and J. J. Baumberg, *Opt. Express*, 2011, **19**, 11256–11263.
56 N. N. Lal, H. Zhou, M. Hawkeye, J. K. Sinha, P. N. Bartlett, G. A. J. Amaratunga and J. J. Baumberg, *Phys. Rev. B: Condens. Matter Mater. Phys.*, 2012, **85**, 245318.
57 J. H. Huang, C. Y. Hsu, C. W. Hu, C. W. Chu and K. C. Ho, *ACS Appl. Mater. Interfaces*, 2010, **2**, 351–359.
58 H. Y. Wei, J. H. Huang, K. C. Ho and C. W. Chu, *ACS Appl. Mater. Interfaces*, 2010, **2**, 1281–1285.

